



# Conceptual design of a Cs<sub>2</sub>LiLaBr<sub>6</sub> scintillator-based neutron total cross section spectrometer on the back-n beam line at CSNS

Da-Jun Zhao<sup>1</sup> · Song Feng<sup>1</sup> · Pin-Jing Cheng<sup>1</sup> · Rong Liu<sup>2</sup> · Wen Luo<sup>1</sup> · Hao-Qiang Wang<sup>1</sup> · Jie-Ming Xue<sup>1</sup> · Kun Zhu<sup>1</sup> · Bo Zheng<sup>1</sup>

Received: 4 September 2022 / Revised: 25 October 2022 / Accepted: 3 November 2022 / Published online: 6 January 2023

© The Author(s), under exclusive licence to China Science Publishing & Media Ltd. (Science Press), Shanghai Institute of Applied Physics, the Chinese Academy of Sciences, Chinese Nuclear Society 2023

## Abstract

To reduce the experimental uncertainty in the <sup>235</sup>U resonance energy region and improve the detection efficiency for neutron total cross section measurements compared with those obtained with the neutron total cross section spectrometer (NTOX), a dedicated lithium-containing scintillation detector has been developed on the Back-n beam line at the China Spallation Neutron Source. The Fast Scintillator-based Neutron Total Cross Section (FAST) spectrometer has been designed based on a Cs<sub>2</sub>LiLaBr<sub>6</sub> (CLLB) scintillator considering the  $\gamma$ -ray flash and neutron environment on the Back-n beam line. The response of the CLLB scintillator to neutrons and  $\gamma$ -rays was evaluated with different <sup>6</sup>Li/<sup>7</sup>Li abundance ratios using Geant4. The neutron- $\gamma$  discrimination performance of the CLLB has been simulated considering different scintillation parameters, physical designs, and light readout modes. A cubic <sup>6</sup>Li-enriched (> 90%) CLLB scintillator, which has a thickness of 4–9 mm and side length of no less than 50 mm to cover the  $\Phi$ 50 mm neutron beam at the spectrometer position, has been proposed coupling to a side readout SiPM array to construct the FAST spectrometer. The developed simulation techniques for neutron- $\gamma$  discrimination performance could provide technical support for other neutron-induced reaction measurements on the Back-n beam line.

**Keywords** Neutron total cross section · CLLB scintillator · Geant4 · Pulse shape discrimination (PSD)

## 1 Introduction

The neutron total cross section is a basic quantity describing the sum of the probabilities of interactions between an incident neutron and nucleus over a unit target area [1]. It plays a significant role in the development of nuclear energy systems [2] and fundamental nuclear physics [3]. Pulsed white neutron sources and advanced spectrometers are essential

for measuring high-quality neutron total cross sections. The Back-n white neutron beam line, which utilizes back-streaming neutrons through the incoming proton channel at the spallation target station of the China Spallation Neutron Source (CSNS) [4, 5], can deliver high-intensity neutrons with an energy spectrum spanning 0.5 eV–200 MeV. A good time resolution related to time-of-flight (TOF) measurements makes Back-n a merit platform for neutron-induced cross section measurements with high accuracy over a wide energy range. The current neutron total cross section spectrometer installed on the Back-n beam line is NTOX, which is based on a multi-cell fission chamber with a maximum of 8 <sup>235</sup>U and <sup>238</sup>U cells [6, 7] and has been successfully applied for neutron total cross section measurements [8–10].

The neutron total cross section is usually obtained by measuring the neutron flux with and without the sample to determine the neutron transmission characteristics at a certain energy, along with considering the sample thickness and nuclei density. A pulsed neutron source combined with the TOF technique allows neutron total cross section data to be measured over a wide energy range. The fission cross

---

This work was supported by the Key Laboratory of Nuclear Data Foundation (No. JCKY2022201C153), National Natural Science Foundation of China (No. 11505216), Educational Commission of Hunan Province of China (No. 19B488), and Natural Science Foundation of Hunan Province of China (Nos. 2021JJ40444 and 2020RC3054).

---

✉ Song Feng  
fengs9115@gmail.com

<sup>1</sup> School of Nuclear Science and Technology, University of South China, Hengyang 421001, China

<sup>2</sup> Institute of Nuclear Physics and Chemistry, China Academy of Engineering Physics, Mianyang 621900, China

section of  $^{235}\text{U}$ , which is the basis for determining fission events and energy of incident neutrons, has a strong resonance effect in the eV–keV energy range [11]. This could cause worse accuracy and enlarge the experimental uncertainty in the neutron total cross section measurements of nuclides with resonance peaks in the same energy region. In addition, the detection efficiency of the multi-cell fission chamber is limited because of the low quantities of  $^{235}\text{U}$ , while increasing  $^{235}\text{U}$  cells is costly and challenging for data analysis. Therefore, a lithium-containing scintillation detector has been proposed as an upgraded spectrometer for neutron total cross section measurements owing to the high and smooth cross sections of  $^6\text{Li}(n,\alpha)\text{T}$  reaction.

At GELINA, the Geel Electron LINear Accelerator facility located in Belgium, Li-glass detectors, plastic scintillators and NE213 scintillators have been applied for neutron total cross section measurements at flight paths with distances from the target up to 400 m [12, 13]. As a shadow bar made of Cu/Pb was placed close to the uranium target to reduce the  $\gamma$ -ray flash and fast neutron component, the background was significantly decreased for neutron measurements using these scintillators along with a  $^{10}\text{B}$  overlap filter close to the sample position for slow neutron absorption. At the photoneutron source (PNS) nELBE, a very compact neutron time-of-flight (nToF) system installed at the superconducting electron linear accelerator with high brilliance and low emittance (ELBE), a plastic scintillator (Eljen EJ-200) has been used for transmitted neutrons detection together with a 3 cm thick lead alloy ( $\text{PbSb}_4$ ), which was used to reduce the bremsstrahlung count rate [14, 15]. Similar spectrometers (e.g.,  $^6\text{LiF}(\text{ZnS})$  scintillators used in the PNS at SINAP [16] and at the Pohang neutron facility (PNF)[17], GS20  $^6\text{Li}$ -glass scintillator at the KURNS-LINAC facility [2], and BC404 scintillator at the weapons neutron research (WNR) facility at LANSCE [1]) have been applied for neutron total cross section measurements based on different types of scintillators considering the neutron beam characterization and radiation environment along with some filters.

In general, organic scintillators are used for fast neutron detection (100 keV–MeV) and inorganic scintillators are used to measure low-energy neutrons (<100 keV). Therefore, measuring the neutron total cross section over a wide energy range (e.g., eV–MeV) usually requires more than one detector and decreases the experimental efficiency as the measurement time is longer. Moreover, experimental uncertainty analysis is challenging, particularly when the results obtained in the same energy range are very different. On the other hand, the Back-n beam line faces the spallation target directly with only a Gd filter placed in front of the samples for very low-energy neutron absorption to inhibit neutrons with different pulses

from overlapping. The strong  $\gamma$ -ray flash, which is a beam of prompt  $\gamma$ -rays produced simultaneously with spallation neutrons, could result in any scintillator working failure within a short time duration. Considering these factors, a physical design and detailed simulations of the lithium-containing scintillator in such an environment is first required to fulfill the requirements before constructing it for neutron total cross section measurements.

In this study, the design criteria for the physical design were first summarized based on the experimental requirements. The  $\text{Cs}_2\text{LiLaBr}_6$  (CLLB) scintillator was proposed for the Fast Scintillator-based Neutron Total Cross Section (FAST) spectrometer design and detailed simulations of the scintillator were performed using Geant4 for detector performance evaluation in terms of detection efficiency and neutron- $\gamma$  discrimination. The conceptual design was analyzed and discussed.

## 2 Simulation of detector response

### 2.1 Experimental requirements and design criteria

The CSNS produces neutrons via proton-induced spallation on a tungsten target. The incident protons are in two bunches, approximately 50 ns wide and 410 ns apart and accelerated through a Linac and synchrotron up to 1.6 GeV with a frequency of 25 Hz and beam power of 125 kW (from Spring 2022). The Back-n neutron beam line is located in the opposite direction of the incident proton beam to the target [4]. Two experimental stations, approximately 55 m and 76 m away from the spallation target, have been installed for nuclear data measurements, irradiation tests, detector calibrations, neutron imaging, and element analysis [5].

In neutron total cross section measurements, samples are placed in the endstation 1 (ES#1) and spectrometer is placed in the endstation 2 (ES#2) to reduce scattering neutrons from the samples, as shown in Fig. 1. Neutrons are well collimated before arriving at the two stations,

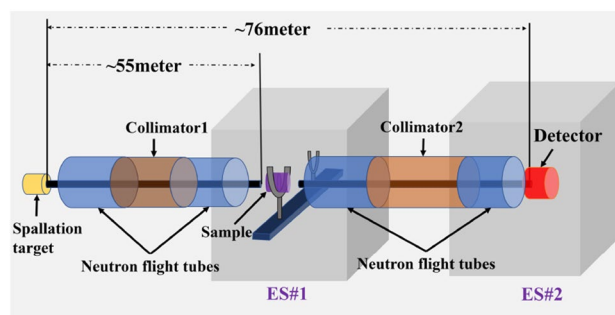


**Fig. 1** (Color online) Schematic of the experimental arrangement for neutron total cross section measurements on the Back-n beam line

and the beam spot at the spectrometer position is available in two sizes:  $\Phi 30$  mm and  $\Phi 50$  mm. Considering the experimental conditions, some essential criteria and requirements must be addressed in the conceptual design of the FAST spectrometer.

- Fast response under strong  $\gamma$ -ray flash irradiation** The  $\gamma$ -ray flash has a relatively strong intensity at the spectrometer position with a  $\Phi 30$  mm or  $\Phi 50$  mm neutron beam. Scintillators are usually sensitive to  $\gamma$ -rays and will reach a saturation level over a period of time to prevent their detection after arriving at fast neutrons. In this case, scintillators with fast timing response and photodetectors (e.g., photomultiplier tube (PMT) or silicon photomultiplier (SiPM)) with good recovery ability are required. Furthermore, the effect of irradiation on the photodetector should be considered when placing it on the rear side of the scintillator.
- Sensitivity to both slow and fast neutrons** Lithium-containing scintillators are common as slow neutron detectors because of the high cross sections of  ${}^6\text{Li}(n,\alpha)\text{T}$  reaction in the low-energy range. However, the measured neutron energy spectrum of Back-n ES#2 ranging from 1 eV to 100 MeV highlights a main component in the MeV region [18]. To maintain the stable response of the scintillator to both slow and fast neutrons, the ratio of  ${}^6\text{Li}$  to  ${}^7\text{Li}$  in lithium should be investigated to improve the experimental efficiency.
- Merit neutron- $\gamma$  discrimination performance in a wide energy range** The  ${}^6\text{Li}(n,\alpha)\text{T}$  reaction proceeds only to the ground state of the product, and the large  $Q$ -value of the reaction allows for merit discrimination of slow neutrons and  $\gamma$ -rays [19]. Scattering  $\gamma$ -rays and  $\gamma$ -rays produced by neutron activation on the spallation target and samples interferes with neutron detection over the entire energy region. Therefore, the neutron- $\gamma$  discrimination capability of lithium-containing scintillator should be investigated in terms of their thickness, geometry, scintillation properties, and readout modes.
- Photodetector protection from radiation** Photodetectors coupled to lithium-containing scintillators can be either PMTs or SiPMs. A SiPM is a matrix of avalanche photodiodes connected in parallel with each other, operating above the breakdown voltage and in Geiger mode [20]. Radiation damage is a major concern when operating these devices in harsh radiation environments [21]. Considering the high flux and high-energy neutrons and  $\gamma$ -rays guided at ES#2, the photodetectors should be well protected from radiation. The side readout of the scintillation light could be a good choice; however, the light collection efficiency should be investigated to ensure that the pulse shape is smooth enough for pulse shape discrimination (PSD) analysis.

New  ${}^6\text{Li}$ -enriched elpasolite crystals (CLYC, CLLB, CLLC, etc.) can detect both neutrons and  $\gamma$ -rays and distinguish between them clearly [22–25]. The CLLB scintillator has a higher light yield (40,000 photons/MeV) than other scintillators of the same type, providing a better signal shape for PSD in the side readout design (which is discussed in Sect. 2.4.3). The CLLB scintillator has a very high thermal neutron reaction cross section and can release up to 4.78 MeV energy through the  ${}^6\text{Li}(n,\alpha){}^3\text{H}$  reaction, ensuring that the CLLB attains a good neutron response and excellent neutron- $\gamma$  discrimination performance. Therefore, the CLLB scintillator was selected as the reference for the conceptual design of the FAST spectrometer.

## 2.2 Simulation model and validation

The scintillator should be sufficiently large to cover the neutron beam in neutron total cross section measurements. As the crystal growth and fabrication process for producing a large inorganic scintillator is challenging, a CLLB scintillator with dimension of 50.8 mm (2 in)  $\times$  50.8 mm  $\times$  6 mm was initially considered. A CLLB model (see Fig. 2) was built in GEANT4 [26, 27] to simulate its response to neutrons. The same model was built in the MCNP to validate the simulation model. The CLLB scintillator was set with a density of 4.2 g/cm<sup>3</sup> and covered by a 1 mm thick aluminum shell. Simulations based on MCNP along with the ENDF/B-VIII.0 library were carried out by counting the (n, $\alpha$ ) reaction events with the FM4 card, whereas simulations based on the Geant4.11.1 version with the FTFP\_BERT\_HP physical model were performed by recording the counts of produced secondary  $\alpha$  particles.

The simulation results of the CLLB neutron detection efficiency using Geant4 and MCNP were compared with each other, as shown in Fig. 3. The ratios of the results simulated by Geant4 to MCNP (G/M) were nearly the same, indicating that the calculated detection efficiencies were well matched when the statistics were sufficiently high. Some small drops were observed in the detection efficiency curve

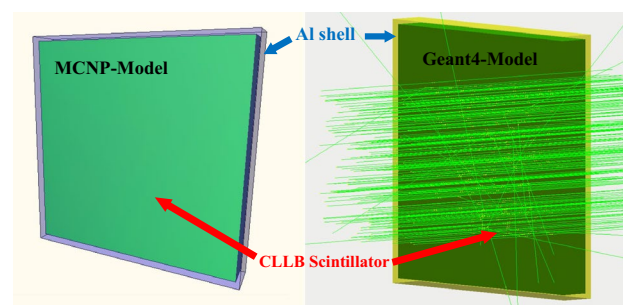
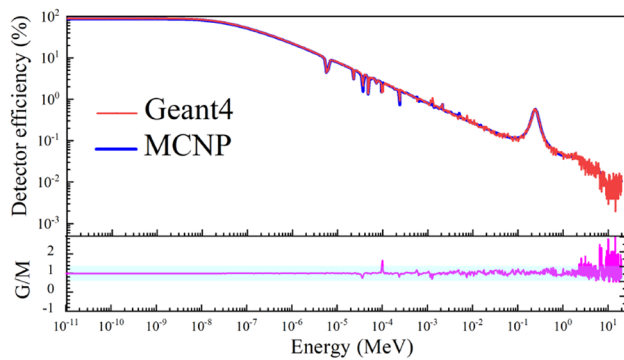


Fig. 2 (Color online) Left: MCNP model. Right: Geant4 model



**Fig. 3** (Color online) Comparison of the CLLB neutron detection efficiency using Geant4 (red line) and MCNP (blue line)

over the eV–keV region, which were mainly caused by competing reactions of Cs, La, and Br in the CLLB scintillator.

### 2.3 Detection efficiency

To minimize the effect induced by  $\gamma$ -ray flash on the CLLB, the  $\gamma$ -ray detection efficiency of the CLLB must be reduced. The scintillator should be thin enough while simultaneously limiting the neutron detection efficiency. The energy deposition response of the CLLB scintillator to neutrons and  $\gamma$ -rays with different thicknesses and  ${}^6\text{Li}/{}^7\text{Li}$  abundance ratios was evaluated. Figure 4 depicts a comparison of CLLB neutron detection efficiency with different  ${}^6\text{Li}/{}^7\text{Li}$  abundance ratios, which confirms that increasing the  ${}^6\text{Li}$  enrichment improves the neutron detection efficiency significantly over the entire energy range. To improve neutron detection efficiency, the  ${}^6\text{Li}$  abundance should be higher than 90%. A 95%  ${}^6\text{Li}$  enrichment was set for the following simulations.

Figure 5 depicts the simulation results of the CLLB response to Back-n neutrons and  $\gamma$ -rays by multiplying the detection efficiency and original energy spectra at the spectrometer position (ES#2). Neutron counts only considered ( $n, \alpha$ ) reactions, and the  $\gamma$ -ray detection efficiency

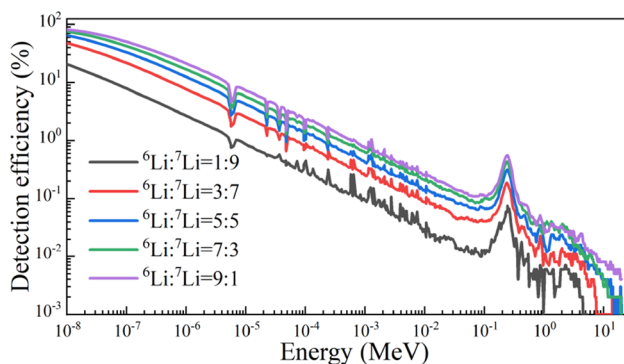


**Fig. 4** (Color online) Detection efficiency simulation results as a function of neutron energy with different  ${}^6\text{Li}/{}^7\text{Li}$  abundance ratios

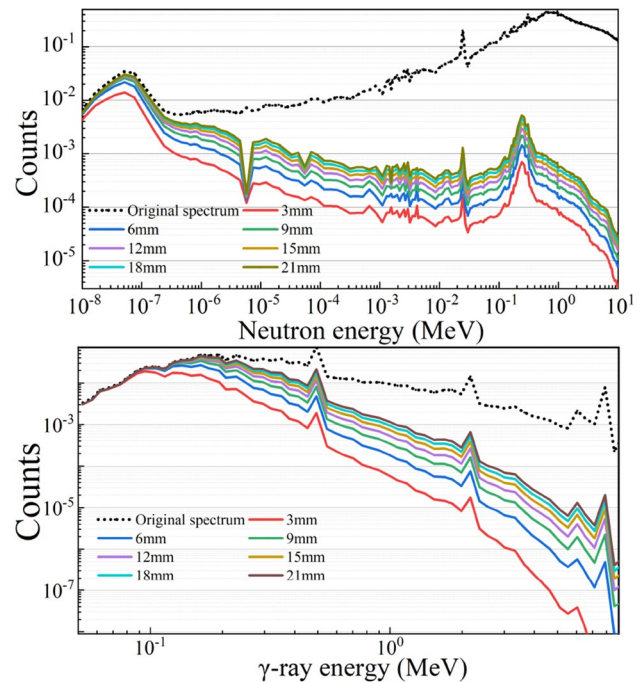


**Fig. 5** (Color online) Simulation results of the CLLB response to Back-n neutrons and  $\gamma$ -rays with different thicknesses. Up: Response to the neutron spectrum. Down: Response to  $\gamma$ -ray energy spectrum

corresponds to the peak detection efficiency. The in-beam  $\gamma$ -ray energy spectrum was extracted from reference [28]. The neutron detection efficiency of the CLLB decreases exponentially with the neutron energy, as shown in Fig. 4. However, as keV–MeV neutrons contribute the main component of the neutron energy spectrum (black dashed line shown in Fig. 5, Up), the response of the CLLB to neutrons on the Back-n beam line does not change significantly over the entire energy range. Figure 5 (Down) shows a similar simulation with the in-beam  $\gamma$ -ray energy spectrum of Back-n (black dash line). The response of the CLLB to  $\gamma$ -rays on the Back-n beam line drops rapidly as a function of energy. The  $\gamma$ -ray detection efficiency of the CLLB was calculated to be sensitive to thickness; accordingly, thin scintillators (3–6 mm) attained a detection efficiency 1–2 orders lower than that of thick ones (12–21 mm).

To identify a suitable thickness to achieve a compromise between high neutron detection and low  $\gamma$ -ray detection, the ratio of detected neutrons to  $\gamma$ -rays ( $n/\gamma$  in following) as a function of the time-of-flight (ns) was calculated for different CLLB thicknesses, as shown in Fig. 6. A double-bunch structure of the neutron beam was considered. The neutron TOF spectrum was first derived from the neutron energy spectrum extracted from reference [4] and then obtained by summing the two identical TOF spectra with a time interval of 410 ns. The double-bunch structure of  $\gamma$ -ray TOF spectrum was extracted from [28].  $n/\gamma$  is the neutron TOF

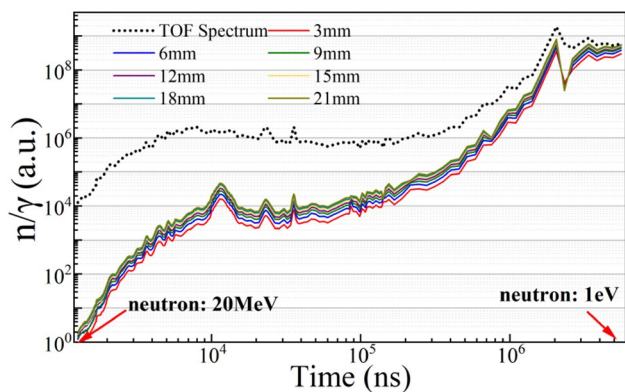


**Fig. 6** (Color online)  $n/\gamma$  ratios of CLLB response to neutrons and  $\gamma$ -rays with different thicknesses and original spectrum

spectrum divided by the  $\gamma$ -ray TOF spectrum (dashed line), considering the CLLB detection efficiency for neutrons and  $\gamma$ -rays (solid lines). Figure 6 shows that the detected  $n/\gamma$  decreases with neutron energy while keeping a relative stable level with CLLB thickness. Considering that high-intensity  $\gamma$ -ray flash is followed by high-energy neutrons, the low detection efficiency of  $\gamma$ -rays will be better; subsequently, a thin CLLB scintillator (e.g., 3 mm) will be the preferred choice for  $\gamma$ -ray suppression. Even though a CLLB scintillator containing highly enriched <sup>6</sup>Li has been proposed for high detection efficiency, its capability for neutron- $\gamma$  discrimination needs to be investigated.

## 2.4 Neutron- $\gamma$ discrimination

### 2.4.1 Pulse shape simulation

In a typical pulse generated by a CLLB scintillator, the decay component of the scintillation light can usually be described by the sum of two exponential functions, as shown in Eq. (1).

$$I(t) = I_f e^{-t/\tau_f} + I_s e^{-t/\tau_s}, \tag{1}$$

where  $I_s$  and  $I_f$  denote the scintillation intensities of the slow and fast components, respectively, and  $\tau_s$  and  $\tau_f$  denote decay time constants of the slow and fast components, respectively. Secondary charged particles produced by neutrons and  $\gamma$ -rays have different ionization energy loss rates ( $-dE/dx$ ), resulting in luminescence decay curves with different fast and slow components for the PSD of neutrons and  $\gamma$ -rays, as shown in Fig. 7.

The scintillation light pulse shape as a function of time was simulated because Geant4 contains the physical process for optical photon transportation [29]. A reflective layer was built with an aluminum foil covering the CLLB scintillator. The optical characteristics of various materials

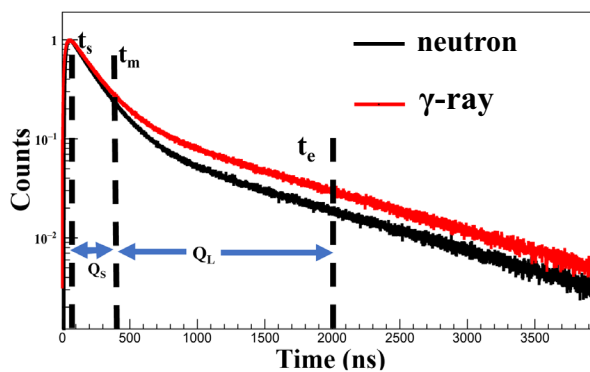


**Fig. 7** (Color online) A typical simulated neutron pulse compared with a normalized  $\gamma$ -ray pulse

must be specified in the optical simulations. A quartz glass window and photocathode material were added to the light output surface, allowing optical photons to be transported through the quartz glass window to the photocathode and converted into electrons through the photoelectric effect. The light emission spectrum of the CLLB was extracted from the research conducted by Shirwadkar et al. [30]. The refractive index and absorption length curves for all materials as a function of photon wavelength were inserted using the AddProperty function. Other physical parameters of the CLLB scintillator were set via the AddConstProperty function, namely, the light yield (40,000 photons/MeV), fast (180 ns) and slow (1080 ns) decay times, and ratios of fast to slow components for neutrons (50:50) and  $\gamma$ -rays (61:39). The interface between different materials and optical properties of the interface were set [29], including the surface types, models, finishes, and reflections (e.g., the surface type between the aluminum shell and the CLLB crystal was set as dielectric\_metal, surface model was set to a glisur model, finish was set to polished, and reflectivity was set to 1).

A typical surface Cf-252 source with a diameter of 50 mm was built to generate neutrons and  $\gamma$ -rays. The  $\gamma$ -ray and neutron emission spectra are described by Eq. (2) and Maxwell's distribution [31], respectively. A 4 mm thick high-density polyethylene (HDPE) was used to slow down fast neutrons for a high detection efficiency.

$$f(E) = \begin{cases} 38.13E_n e^{1.648E_n} & E_n \leq 0.3 \\ 26.8E_n e^{-2.3E_n} & 0.3 < E_n \leq 1.0 \\ 8.0E_n e^{-1.1E_n} & E_n > 1 \end{cases} \tag{2}$$

The light pulse of each event was simulated by counting the time distribution of all photons arriving at the photocathode. To simulate the electric pulse, the number of photons within each time bin of the light pulse was converted to the number of electrons by calculating the convolution of the

photon energy distribution and photon detection efficiency curve of the photocathode. The quantum efficiency of the HAMAMATSU MPPC-S14160 SiPM was applied. A typical simulated neutron pulse is compared with an amplitude-normalized  $\gamma$ -ray pulse in Fig. 7.

### 2.4.2 PSD analysis

The simulated neutron- $\gamma$  discrimination performance of the CLLB scintillator was evaluated based on PSD analysis. The charge comparison (CC) [32] method was applied to compare the charge differences over the tail of the pulses by calculating the CC factor as a function of energy. The CC factor corresponds to the ratio of the long integration  $Q_L$  from  $t_m$  to  $t_e$  to the short integration  $Q_S$  from  $t_s$  to  $t_e$  of the pulse, as illustrated in Fig. 7. The figure of merit (FoM) [33] is defined using Eq. (3) for quantitative evaluation.

$$\text{FoM} = \frac{S}{\text{FWHM}_n + \text{FWHM}_\gamma} \quad (3)$$

Here,  $S$  is the separation between two peaks attributed to neutrons and  $\gamma$ -rays.  $\text{FWHM}_n$  and  $\text{FWHM}_\gamma$  represent the full width at half maximum (FWHM) of the two peaks, respectively.

Figure 8 shows the 2D histograms of the neutron- $\gamma$  discrimination and corresponding neutron and  $\gamma$ -ray pulse height spectra with and without a 4 cm thick HDPE moderator, respectively. The distribution of fast neutron events is a continuum, with a response of 4.78 MeV plus incident fast neutron kinetic energy. However, the distribution of thermal neutron events is concentrated at approximately 4.78 MeV. A similar experimental result was obtained in reference [34] on the  ${}^6\text{Li}(n, \alpha)$  reaction response and PSD performance of a CLYC scintillator. The CLLB scintillator attains an excellent PSD performance with a FoM value of 1.46 for fast neutrons and 1.42 for moderated neutrons, respectively, cutting the red area for event selection, as shown in Fig. 8.

### 2.4.3 Analysis of influencing factors on PSD performance

- Scintillator shape and thickness** Cylindrical inorganic scintillators are commonly used commercially and are usually coupled with a photodetector that detects scintillation light from the rear side. A cubic scintillator is easier for side readout; however, its light collection efficiency and uniformity should be investigated. To compare the PSD performance with different scintillator shapes and thicknesses, the neutron- $\gamma$  discrimination performance of a cylindrical scintillator ( $\Phi$  50.8 mm) and cubic scintillator (50.8 mm  $\times$  50.8 mm) with different

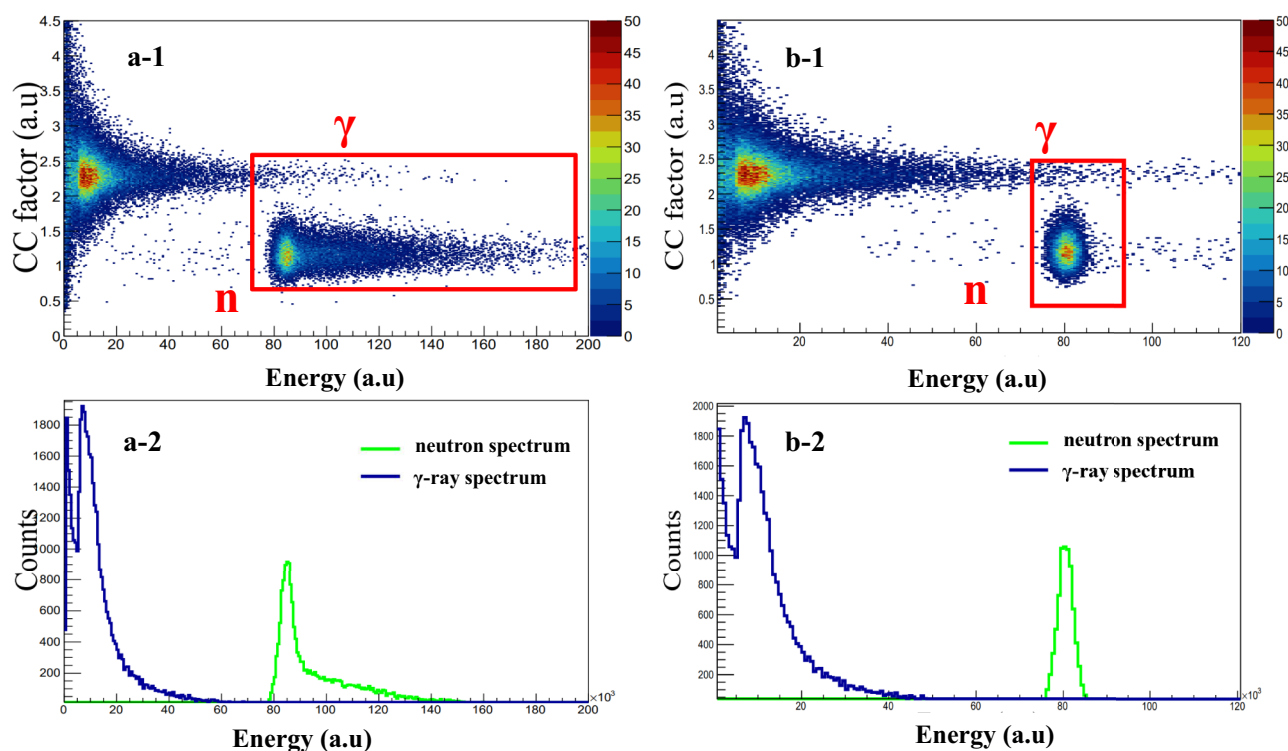


**Fig. 8** (Color online) 2D histograms of the neutron- $\gamma$  discrimination (up) and corresponding energy spectra (down). Left panel: without a HDPE moderated Cf-252 source. Right panel: with a HDPE moderator

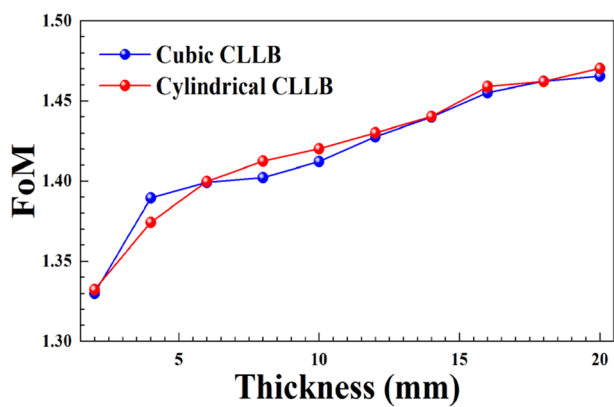


Fig. 9 (Color online) FoM results as a function of the CLLB thickness with different shapes

thicknesses were simulated and analyzed. Figure 9 shows the FoM values as a function of thickness for cylindrical and cubic scintillators, revealing that the PSD performance of the cubic scintillator agrees well with that of the cylindrical one. The FoM values were found to increase significantly from 2 to 4 mm and then increased slowly. The main reason for this could be that the thermal neutron absorption length of the high <sup>6</sup>Li-enriched CLLB scintillator is approximately 3 mm [35]. Considering the required PSD quality in the low-energy range, the thickness of the CLLB scintillator should be greater than 3 mm.

- **Proportions of fast and slow scintillation components**  
We found that changing the fast component proportion of the CLLB scintillation light has a significant impact on its PSD performance [36]. Figure 10 shows the relative

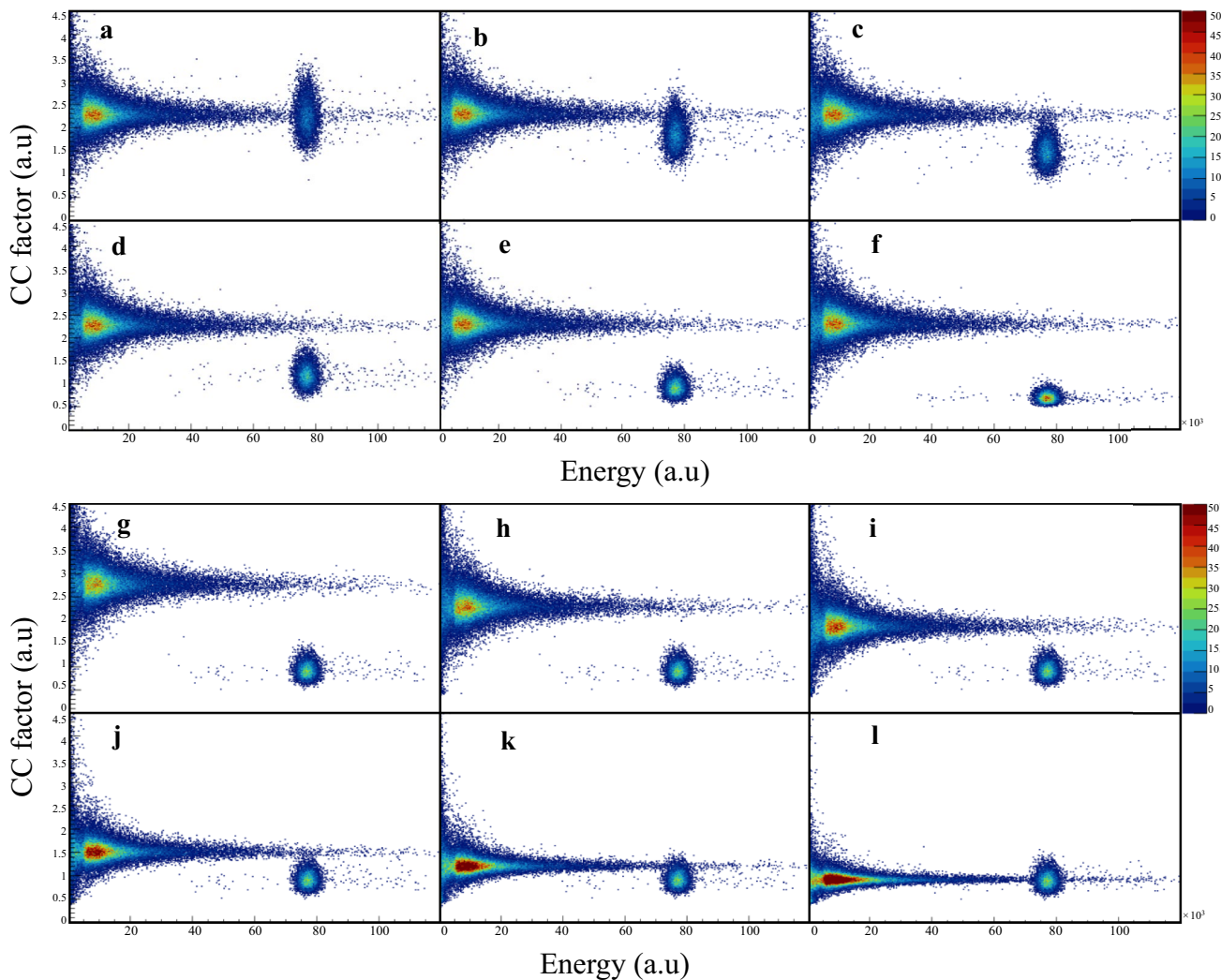


Fig. 10 (Color online) 2D histogram of simulated neutron- $\gamma$  discrimination with different fast component proportions in pulses generated by neutrons (upper panel) and  $\gamma$ -rays (bottom panel). a–f: proportions

ranging from 40% to 90% with an interval of 10%. g–l: proportions ranging from 30% to 80% with an interval of 10%

position distribution of neutrons and  $\gamma$ -rays in the 2D histogram of PSD when different fast scintillation components were set for neutrons and  $\gamma$ -ray. Figure 10 (a–f) corresponds to the PSD simulation results with changing the fast scintillation component proportions (40–90%) for neutrons only. A large fast component of the scintillation light generated by neutrons could improve PSD

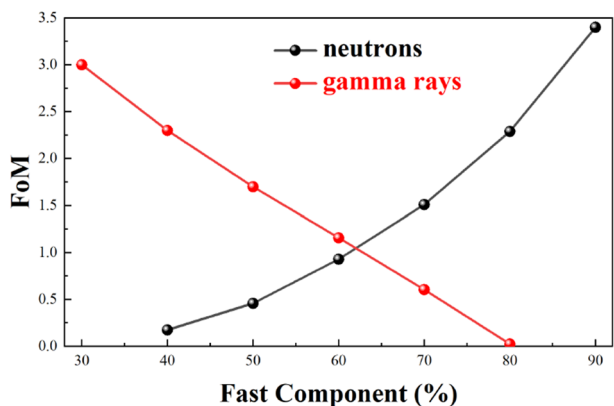


Fig. 11 (Color online) FoM results as a function of fast component ratio of neutron and  $\gamma$ -ray

significantly, as shown in Fig. 11 (black line). In contrast, the performance of the PSD decreases rapidly with an increasing share of the fast scintillation component for  $\gamma$ -rays, as underlined by the red line, which was obtained using the simulation results presented in Fig. 10 (g–l). Accurate proportions of the fast and slow components of the scintillation light generated by neutrons and  $\gamma$ -rays are proven to be critical in PSD simulation, which provides a reference for achieving better PSD performance in elpasolite crystal design.

- Readout modes** To protect the photodetector from the irradiation of high-intensity neutrons and  $\gamma$ -rays, the side readout should be prior to the rear readout in the physical design of the FAST spectrometer. The scintillation light collection and PSD performance were calculated with different readout modes using a moderated Cf-252 neutron source. Figure 12 shows the models built in Geant4 and corresponding 2D histogram of PSD performance, from which note that the side readout mode collects fewer photons than the rear readout. This is because the photons have a longer transportation path through the scintillator in the side readout model and collecting area is also lower than that in the rear readout model, resulting in some optical photons being self-absorbed by the

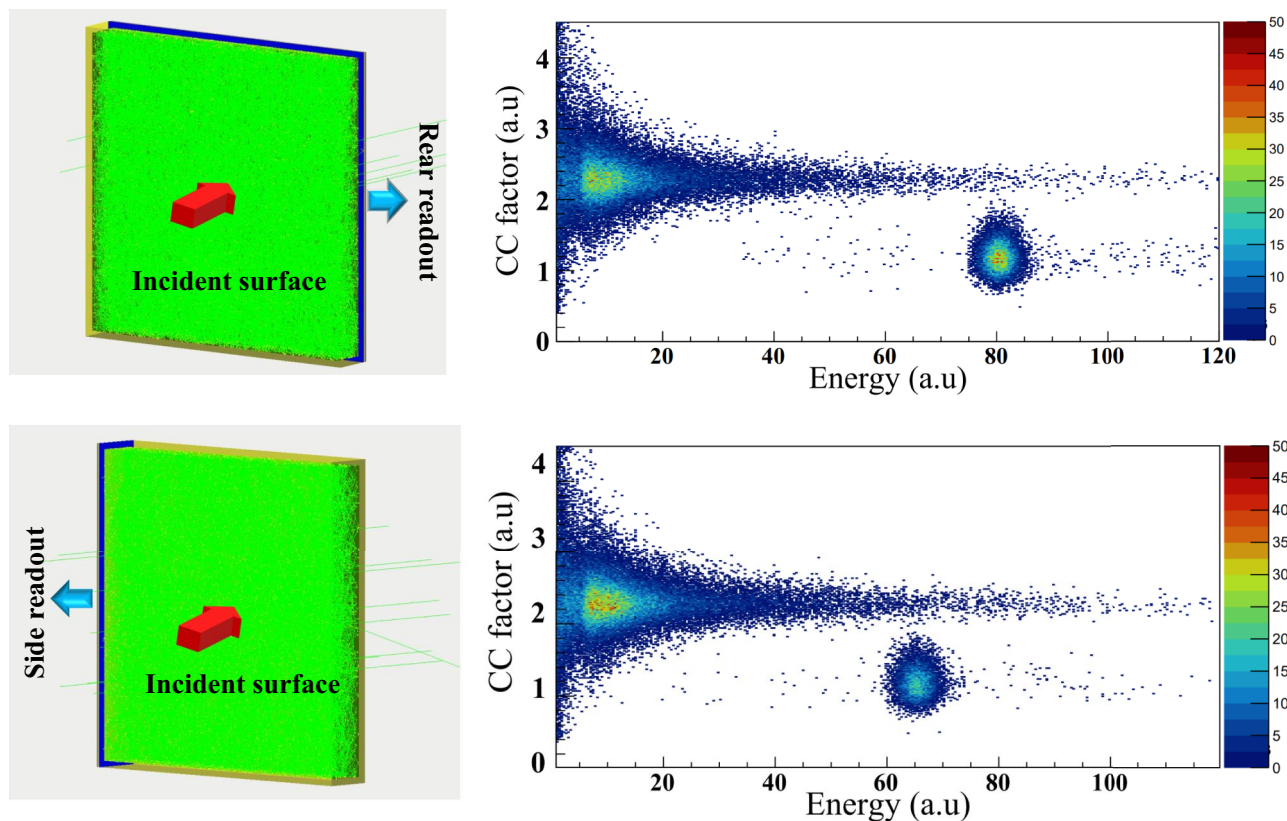


Fig. 12 (Color online) Comparison of scintillation light collection models and corresponding 2D histograms of PSD simulations with rear (Up) and side readouts (Down)

scintillator itself. However, the PSD performances of the two models were comparable, attaining an FoM of 1.44 with the rear readout compared with an FoM of 1.42 using the side readout model.

### 3 Discussion

The physical design of a CLLB scintillator-based spectrometer for neutron total cross section measurements includes determining the readout mode and physical parameters of the scintillator, that is, scintillator area, thickness, <sup>6</sup>Li enrichment, Ce-doping percentage, and PSD performance in the energy range of interest. With calculations performed using the Geant4 code on the detection efficiency of neutrons, a high <sup>6</sup>Li-enriched (>90%) CLLB scintillator has been proposed for a higher neutron detection efficiency in 1 eV to 10 MeV energy range. A thin CLLB scintillator is the preferred choice based on the calculations regarding the n/γ ratios of the CLLB response to neutrons and γ-rays considering the Back-n neutron and γ energy spectra. However, thin CLLB scintillators exhibit poor neutron-γ discrimination performance. As a compromise, a 4–9 mm thick CLLB scintillator has been recommended for the FAST spectrometer design; however, the final size depends on the crystal growth and fabrication level. To achieve a better neutron-γ discrimination performance, the fast component of the scintillation light generated by neutrons should be as high as possible, whereas γ-rays require a low fast scintillation component. The proportion of the fast component in the scintillation light generated by neutrons can be adapted with the Ce-doping percentage [36]. As the PSD performance changes slightly with the side readout compared with the rear readout, an array of SiPMs is designed coupled to the side of a CLLB scintillator for radiation protection. The inherent fast rise time of the SiPM owing to the avalanche characteristics of the pixels, makes it ideal for counters in TOF spectrometers [37, 38]. In practice, a gated technique [39] and shadow bar can be applied for spectrometer response recovery and γ-ray flash reduction. In the future, a calibration experiment based on a neutron generator should be performed to validate simulations dedicated to the physical design of the FAST spectrometer.

### 4 Conclusion

To design a Fast Scintillator-based Neutron Total Cross Section (FAST) spectrometer on the Back-n beam line at CSNS, a detailed simulation of the CLLB response to neutrons and γ-rays was performed using the Geant4 toolkit.

The detection efficiency of a CLLB scintillator was investigated as a function of <sup>6</sup>Li abundance; consequently, a high <sup>6</sup>Li-enriched (95%) CLLB scintillator was applied to simulate the thickness characteristics and PSD performance. The PSD performances of CLLB scintillators with varying thicknesses were simulated with a standard Cf-252 neutron source and quantum efficiency curve of a commercial SiPM. The influences of different shapes, thicknesses, proportions of fast components in scintillation light, and readout modes were simulated and analyzed. As a result, a final conceptual design of the FAST spectrometer has been proposed based on a 50.8 mm × 50.8 mm cubic scintillator to cover the Φ50 mm neutron beam line on the Back-n beam line. The cubic CLLB is high <sup>6</sup>Li-enriched (>90%), 4–9 mm thick, and capable of high neutron-γ discriminating performance (FoM>1.3 for thermal neutrons). An array of SiPMs coupled to a CLLB scintillator with side readout is considered for radiation protection, and a benchmarking experiment for validating simulations with a neutron generator is recommended in the future. The simulations, especially the technique of pulse shape simulation developed for PSD analysis, support the construction of the FAST spectrometer and provide an important reference for similar spectrometer designs on the Back-n beam line.

**Author Contributions** All authors contributed to the study conception and design. Material preparation, data collection and analysis were performed by Da-Jun Zhao, Song Feng, Pin-Jing Cheng, Rong Liu, Wen Luo and Bo Zheng. The first draft of the manuscript was written by Da-Jun Zhao and Song Feng and all authors commented on previous versions of the manuscript. All authors read and approved the final manuscript.

### References

1. W.P. Abfalterer, F.B. Bateman, F.S. Dietrich et al., Measurement of neutron total cross sections up to 560 MeV. *Phys. Rev. C* **63**(4), 044608 (2001). <https://doi.org/10.1103/PhysRevC.63.044608>
2. J. Lee, J. Nishiyama, Jun-Ichi. Hori et al., Neutron total cross section measurements of polyethylene using time-of-flight method at KURNS-LINAC. *J. Nucl. Sci. Technol* **57**(1), 1–8 (2020). <https://doi.org/10.1080/00223131.2019.1647894>
3. S. Kopecky, P. Riehs, J.A. Harvey et al., New measurement of the charge radius of the neutron. *Phys. Rev. Lett.* **74**(13), 2427 (1995). <https://doi.org/10.1103/PhysRevLett.74.2427>
4. Q. An, H.Y. Bai, J. Bao et al., Back-n white neutron facility for nuclear data measurements at CSNS. *J. Instrum.* **12**(07), P07022 (2017). <https://doi.org/10.1088/1748-0221/12/07/P07022>
5. J.Y. Tang, Q. An, J.B. Bai et al., Back-n white neutron source at CSNS and its applications. *Nucl. Sci. Tech* **32**, 11 (2021). <https://doi.org/10.1007/s41365-021-00846-6>
6. J. Wen, Y. Yang, Z. Wen et al., A multi-layered fast ionization chamber prototype for fission cross section measurements. *J. Instrum.* **13**(07), P07020 (2018). <https://doi.org/10.1088/1748-0221/13/07/P07020>
7. Y. Yang, Z. Wen, Z. Han et al., A multi-cell fission chamber for fission cross-section measurements at the back-n white neutron

- beam of CSNS. Nucl. Instr. Methods A **940**, 486–491 (2019). <https://doi.org/10.1016/j.nima.2019.06.014>
8. X.Y. Liu, Y.W. Yang, R. Liu et al., Measurement of the neutron total cross section of carbon at the back-n white neutron beam of CSNS. Nucl. Sci. Tech **30**(9), 139 (2019). <https://doi.org/10.1007/s41365-019-0660-9>
  9. X. Liu, Y. Yang, R. Liu et al., Measurement of the neutron total cross sections of aluminum at the back-n white neutron source of CSNS. Eur. Phys. J. A **57**(7), 1–11 (2021). <https://doi.org/10.1140/epja/s10050-021-00513-9>
  10. J.-L. Zhang, B. Jiang, Y.-H. Chen et al., Measurement of total neutron cross section of natural lithium at China Spallation Neutron Source Back-n facility. Acta Phys. Sin. **71**(5), 052901 (2022). <https://doi.org/10.7498/aps.71.20211646>
  11. Z.G. Ge, R.R. Xu, H.C. Wu et al., CENDL-3.2: The new version of Chinese general purpose evaluated nuclear data library. EPJ Web Conf. **239**, 09001 (2020). <https://doi.org/10.1051/epjconf/202023909001>
  12. W. Mondelaers, P. Schillebeeckx, GELINA a neutron time-of-flight facility for high-resolution neutron data measurements. Res. Infrastr. (2006). <https://publications.jrc.ec.europa.eu/repository/handle/JRC35644>
  13. I. Sirakov, B. Becker, R. Capote et al., Results of total cross section measurements for  $^{197}\text{Au}$  in the neutron energy region from 4 to 108 keV at GELINA. Eur. Phys. J. A **49**, 144 (2013). <https://doi.org/10.1140/epja/i2013-13144-2>
  14. R. Hannaske, Z. Elekes, R. Beyer et al., Neutron total cross section measurements of gold and tantalum at the nELBE photoneutron source. Eur. Phys. J. A **49**, 137 (2013). <https://doi.org/10.1140/epja/i2013-13137-1>
  15. A. Junghans, R. Beyer, J. Claußner et al., Neutron transmission measurements at nELBE. EPJ Web Conf. **239**, 01006 (2020). <https://doi.org/10.1051/epjconf/202023901006>
  16. L.X. Liu, H.W. Wang, Y.G. Ma et al., Measurements of the total cross section of  $^{nat}\text{Be}$  with thermal neutrons from a photo-neutron source. Nucl. Instrum. Methods B **410**, 158–163 (2017). <https://doi.org/10.1016/j.nimb.2017.08.022>
  17. S.G. Shin, Y.-U. Kye, M.-H. Cho et al., Neutron total cross-section measurements with the  $^6\text{Li}$ -Zns (Ag) scintillator (BC702) employing a neutron and noise separation technique. J. Korean Phys. Soc. **64**(9), 1288–1292 (2014). <https://doi.org/10.3938/jkps.64.1288>
  18. Y.H. Chen, G.Y. Luan, J. Bao et al., Neutron energy spectrum measurement of the Back-n white neutron source at CSNS. Eur. Phys. J. A **55**, 115 (2019). <https://doi.org/10.1140/epja/i2019-12808-1>
  19. G.F. Knoll, *Radiation detection and measurement (fourth edition)* (John Wiley & Sons, 2010)
  20. E. Garutti, Yu. Musienko, Radiation damage of SiPMs. Nucl. Instr. Methods A **926**, 69–84 (2019). <https://doi.org/10.1016/j.nima.2018.10.191>
  21. B. Biró, G. David, A. Fenyvesi et al., A comparison of the effects of neutron and gamma radiation in silicon photomultipliers. IEEE Trans. Nucl. Sci. **66**(7), 1833–1839 (2019). <https://doi.org/10.1109/TNS.2019.2921102>
  22. J. Glodo, E. van Loef, R. Hawrami et al., Selected properties of  $\text{Cs}_2\text{LiYCl}_6$ ,  $\text{Cs}_2\text{LiLaCl}_6$ , and  $\text{Cs}_2\text{LiLaBr}_6$  scintillators. IEEE Trans. Nucl. Sci. **58**(1), 333–338 (2011). <https://doi.org/10.1109/TNS.2010.2098045>
  23. R.S. Woolf, E.A. Wulf, B.F. Philips et al., Identification of internal radioactive contaminants in elpasolites (CLYC, CLLB, CLLBC) and other inorganic scintillators. Nucl. Instr. Methods A **954**, 161228 (2020). <https://doi.org/10.1016/j.nima.2018.09.063>
  24. J. Glodo, R. Hawrami, E. van Loef et al., Pulse shape discrimination with selected elpasolite crystals. IEEE Trans. Nucl. Sci. **59**(5), 2328–2333 (2012). <https://doi.org/10.1109/TNS.2012.2188646>
  25. K.-N. Li, X.-P. Zhang, Q. Gui et al., Characterization of the new scintillator  $\text{Cs}_2\text{LiYCl}_6$ : Ce $^{3+}$ . Nucl. Sci. Tech **29**(1), 11 (2018). <https://doi.org/10.1007/s41365-017-0342-4>
  26. S. Agostinelli, J. Allison, Ka. Amako et al., GEANT4—a simulation toolkit. Nucl. Instr. Methods A **506**(3), 250–303 (2003). [https://doi.org/10.1016/S0168-9002\(03\)01368-8](https://doi.org/10.1016/S0168-9002(03)01368-8)
  27. J. Allison, K. Amako, J. Apostolakis et al., Recent developments in Geant4. Nucl. Instr. Methods A **835**, 186–225 (2016). <https://doi.org/10.1016/j.nima.2016.06.125>
  28. J. Ren, X.-C. Ruan, Y.-H. Chen et al., In-beam  $\gamma$ -rays of back-streaming white neutron source at china spallation neutron source. Acta Phys. Sin. **69**(17), 20200718 (2020). <https://doi.org/10.7498/aps.69.20200718>
  29. E. Dietz-Laursonn, Peculiarities in the simulation of optical physics with Geant4, arXiv preprint [arXiv:1612.05162](https://arxiv.org/abs/1612.05162) (2016). <https://doi.org/10.48550/arXiv.1612.05162>
  30. U. Shirwadkar, J. Glodo, E.V. Van Loef et al., Scintillation properties of  $\text{Cs}_2\text{LiLaBr}_6$  (CLLB) crystals with varying  $\text{Ce}^{3+}$  concentration. Nucl. Instr. Methods A **652**(1), 268–270 (2011). <https://doi.org/10.1016/j.nima.2010.08.050>
  31. J. Meadows, Cf 252 fission neutron spectrum from 0.003 to 15.0 MeV. Phys. Rev **157**(4), 1076 (1967). <https://doi.org/10.1103/PhysRev.157.1076>
  32. D. Zhao, S. Feng, C. Hu et al., Characterization of the neutron/ $\gamma$ -ray discrimination performance in an EJ-301 liquid scintillator for application to prompt fission neutron spectrum measurements at CSNS. Radiat. Meas. **151**, 106703 (2022). <https://doi.org/10.1016/j.radmeas.2022.106703>
  33. H. Arahmane, E.M. Hamzaoui, Y. Ben Maissa et al., Neutron-gamma discrimination method based on blind source separation and machine learning. Nucl. Sci. Tech **32**, 18 (2021). <https://doi.org/10.1007/s41365-021-00850-w>
  34. N. D'olympia, P. Chowdhury, C. Lister et al., Pulse-shape analysis of CLYC for thermal neutrons, fast neutrons, and gamma-rays. Nucl. Instr. Methods A **714**, 121–127 (2013). <https://doi.org/10.1016/j.nima.2013.02.043>
  35. P. R. Menge, J. Lejay, V. Ouspenski, Design and performance of a compact  $\text{Cs}_2\text{LiLaBr}_6$ (Ce) neutron/gamma detector using silicon photomultipliers. IEEE Nucl. Sci. Symp. Med. Imaging Conf. Rec. (2015). <https://doi.org/10.1109/NSSMIC.2015.7581858>
  36. K. Yang, P. R. Menge, J. Lejay et al., Scintillation properties and temperature responses of  $\text{Cs}_2\text{LiLaBr}_6$ : Ce  $^{3+}$ . IEEE Nucl. Sci. Symp. Med. Imaging Conf. Rec. 1–6 (2013). <https://doi.org/10.1109/NSSMIC.2013.6829676>
  37. Q. Wang, X. Tuo, C. Deng et al., Characterization of a  $\text{Cs}_2\text{LiYCl}_6$ : Ce $^{3+}$  scintillator coupled with two silicon photomultiplier arrays of different sizes. Nucl. Instr. Methods A **942**, 162339 (2019). <https://doi.org/10.1016/j.nima.2019.162339>
  38. F. Liang, J. Smith, Characterization of CLLBC coupled to silicon photomultipliers. IEEE Trans. Nucl. Sci. **67**(6), 927–932 (2020). <https://doi.org/10.1109/TNS.2020.2988555>
  39. P. Hu, Z.-G. Ma, K. Zhao et al., Development of gated fiber detectors for laser-induced strong electromagnetic pulse environments. Nucl. Sci. Tech. **32**, 58 (2021). <https://doi.org/10.1007/s41365-021-00898-8>

Springer Nature or its licensor (e.g. a society or other partner) holds exclusive rights to this article under a publishing agreement with the author(s) or other rightsholder(s); author self-archiving of the accepted manuscript version of this article is solely governed by the terms of such publishing agreement and applicable law.